GEOPHYSICAL RESEARCH LETTERS, VOL. 33, L16311, doi:10.1029/2006GL026883, 2006

Measuring two-dimensional movements using a single InSAR pair

Noa B. D. Bechor[1] and Howard A. Zebker[1]

Received 1 May 2006; revised 26 June 2006; accepted 12 July 2006; published 23 August 2006.

[1] We present a new method to extract along-track displacements from InSAR data, based on split-beam InSAR processing, to create forward- and backward-looking interferograms. The phase difference between the two modified interferograms provides the along-track displacement component. Thus, from each conventional InSAR pair we extract two components of the displacement vector: one along the line of sight, the other in the along-track direction. We analyze the precision of the new method by comparing our solution to GPS and offset-derived along-track displacements in interferograms of the 1999, Hector Mine earthquake. The RMS error between GPS displacements and our results ranges from 5 to 8.8cm. Our method is consistent with along-track displacements derived by pixel-offsets, which are limited to 12–15cm precision. The theoretical precision of the new method depends on SNR and coherence. For a signal to noise ratio of 30 the expected precisions are 3, 11cm for coherence of 0.8, 0.4, respectively. **Citation:** Bechor, N. B. D., and H. A. Zebker (2006), Measuring two-dimensional movements using a single InSAR pair, *Geophys. Res. Lett.*, *33*, L16311, doi:10.1029/2006GL026883.

1. Introduction

[2] A major limitation of InSAR for geophysical applications is that the technique is only sensitive to one-dimensional motion along the satellite's line of sight (LOS), while most deformation is better characterized using three dimensional geodetic data. Thus, many studies have incorporated multiple radar passes using different geometries to resolve off LOS motions [e.g., *Funning et al.*, 2005; *Fialko*, 2004; *Froger et al.*, 2004; *Joughin et al.*, 1998]. Although these solutions typically provide some separation between spatial deformation components, they cannot span the full 3D space accurately with data acquired by currently operating satellites. A satellite with both left and right looking capability in a non-polar orbit is necessary to fully resolve three-dimensional deformation using conventional InSAR [*Wright et al.*, 2004]. Such satellite designs have been proposed [*Wadge et al.*, 2003, H. Zebker, personal communication, 2006], however their construction offers technical challenges, and these systems are thus expensive. As a result, no left- and right-looking satellite mission is planned for the foreseeable future.

[3] If existing satellites are operated to obtain both ascending and descending radar passes over a single area, two components of deformation may be inferred from the interferogram phases. The third component may be inferred from pixel amplitude offset analysis [*Michel et al.*, 1999a, 1999b], albeit at very reduced sensitivity. In this approach two or more amplitude images are cross correlated piecewise, to obtain a strain image. This method is in fairly wide use [e.g., *Fialko et al.*, 2005; *Simons et al.*, 2002; *Jonsson et al.*, 2002; *Fialko et al.*, 2001; *Peltzer et al.*, 1999]. Studies comparing the amplitude pixel offset analysis with ground truth (GPS data) suggest the method's precision for ERS data with high correlation is limited to ~12–15cm [e.g., *Jonsson et al.*, 2002; *Fialko et al.*, 2001; *Fialko*, 2004]. Because cross-correlation accuracy depends on the size of the correlation windows, there is a trade-off between sensitivity and measurement density.

[4] We propose here a split-beam method, which we denote multiple aperture InSAR (MAI), that is both more efficient and a more accurate measurement of the along-track deformation component than pixel amplitude correlation. When applied to InSAR data acquired over the Hector Mine earthquake, we were able to increase precision by a factor of at least 2 over the results published by *Jonsson et al.* [2002] and *Fialko* [2001]. While there is still a choice between measurement density and accuracy, the new method offers an improvement in precision with significantly reduced computation time.

2. Method

[5] We measure the along-track component of deformation using sub-aperture processing in the along-track direction, thereby constructing forward- and backward-looking interferograms of the ground. The phase difference from the two look directions is proportional to any along-track deformation.

[6] In the forward looking interferogram, the phase corresponds to changes along a LOS slightly forward of the nominal radar squint direction θ_{SQ} (Figure 1). Similarly, the backward-looking interferogram corresponds to deformation along a slightly different LOS. Subtracting the phases produces a phase difference representative of azimuth displacements between radar passes.

[7] Consider a radar sensor with geometry as depicted in Figure 1. Denote the radar nominal 'squint' angle as θ_{SQ}, and the antenna angular beam width by α. To form the forward looking interferogram, we use only the forward part of the antenna beam width, and integrate around a new squint angle, $\theta_{SQ} + \beta$. For simplicity, consider integrating over one half beam width, so $\beta = \frac{\alpha}{4}$. The backward looking interferogram is similarly formed from the back half of the antenna beam. For a displacement x in the along track direction, the interferogram phases Φ are:

$$\Phi_{\text{forward}} = -\frac{4\pi x}{\lambda} \sin\left(\theta_{SQ} + \frac{\alpha}{4}\right) \quad (1)$$

[1]Department of Geophysics, Stanford University, Stanford, California, USA.

0094-8276/06/2006GL026883$05.00

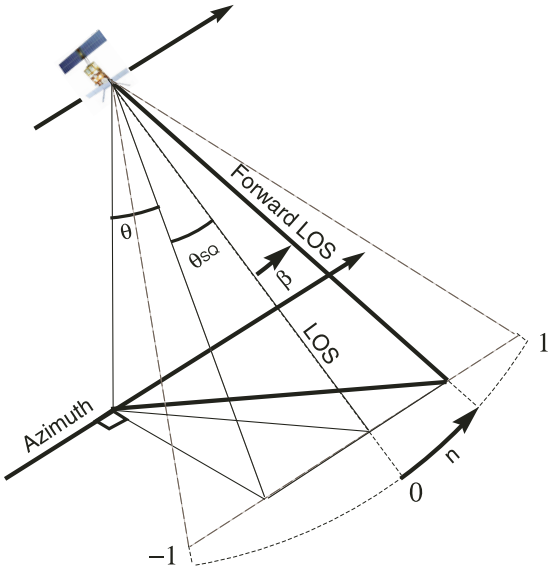

Figure 1. Illustration of MAI imaging geometry. The antenna mid-beam line of sight (LOS) has a 'squint' angle θ_{SQ}. We squint it further by an angle $\pm\beta$, to form forward- and backward-looking interferograms. The angle β is defined as a fraction n of half the beam width. The new along-track resolution is $\frac{l}{2(1-n)}$.

$$\Phi_{back} = -\frac{4\pi x}{\lambda}\sin\left(\theta_{SQ} - \frac{\alpha}{4}\right) \tag{2}$$

$$\Phi_{MAI} = \Phi_{forward} - \Phi_{back} = -\frac{4\pi x}{\lambda} 2\sin\frac{\alpha}{4}\cos\theta_{SQ} \tag{3}$$

where λ denotes wavelength. For small α and θ_{SQ}, $\Phi_{MAI} = \frac{2\pi x}{\lambda}\alpha$. Since $\alpha \approx \frac{\lambda}{l}$, where l is the antenna length:

$$\Phi_{MAI} = \frac{2\pi}{l}x \tag{4}$$

[8] For the ERS satellite $l = 10$ m, and 1 m of along-track displacement yields about 0.6 radians of phase difference.

[9] Inverting and expressing the results in terms of uncertainties,

$$\sigma_x = \frac{l}{2\pi}\sigma_\Phi \tag{5}$$

where σ_Φ and σ_x are the standard deviation of the phase and displacement measurements, respectively.

[10] For an interferogram with a given signal to noise ratio (SNR) and effective number of looks N_L, the phase noise can be approximated by [*Rodriguez and Martin*, 1992]:

$$\sigma_\Phi \approx \frac{1}{\sqrt{2N_L}}\frac{\sqrt{1-\rho^2}}{\rho} \tag{6}$$

where the total correlation $\rho = \frac{|\rho_{spatial,temporal}|}{1+\frac{1}{SNR}}$, with decorrelation sources as defined by *Zebker and Villasenor* [1992].

[11] We note that it is possible to generate the forward- and backward-looking interferograms using only a portion of the available beam width, thereby generating a split aperture wider than $\frac{\alpha}{2}$. To formulate the forward/backward squint β as a function of antenna angular beam width α, we define a normalized squint $n = \frac{2\beta}{\alpha}$, shown in Figure 1. Changing the aperture width has two opposing effects: increasing the phase sensitivity to deformation and reducing the SNR. The SNR decreases because the total along-track integration time decreases. As a result the optimal aperture width is different for different SNR and correlation values. Because the resolution degrades with aperture loss, the effective number of looks is also reduced.

[12] Figures 2a–2c show the theoretical standard deviation of the along-track displacement measurement as a function of normalized squint n for ERS, with various SNR and correlation values. Results for SNR = 316, 31 and 3, with correlation $\rho = 0.2$ to $\rho = 0.8$ are displayed in Figures 3a, 3b, and 3c, respectively. We note that for SNR = 3 the optimal squint is $n = 0.5$, increasing to 0.6 for ten times higher SNR, and to 0.666 for SNR = 316. We assume averaging over 32 × 32 pixel windows. This number refers to pixel averaging and not effective looks: we account for resolution reduction with aperture widening by calculating the effective number of looks to produce Figure 2.

[13] Because the topographic phase contribution is not very sensitive to squint direction, its contribution to the interferometric phase appears in both interferograms. Similarly, the cross-track and vertical components of deformation contributions to phase are identical in the forward and

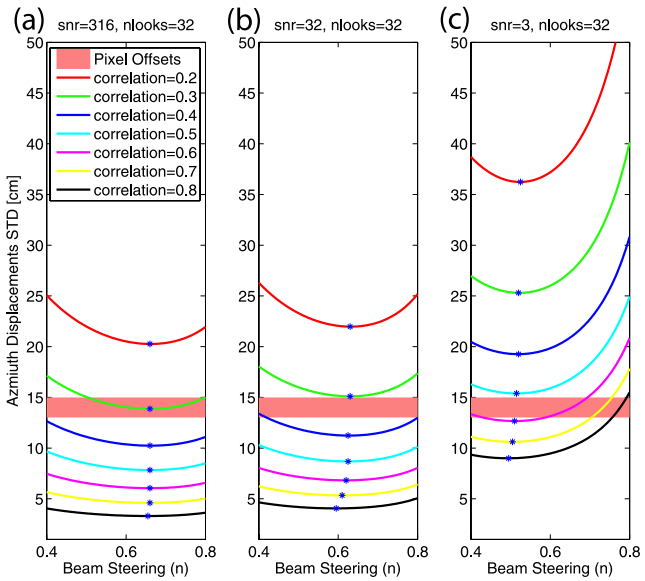

Figure 2. Predicted standard deviation variations. Curves are derived from *Rodriguez and Martin* [1992] and equation (5). We present theoretical precision for correlation values of 0.1 to 0.8, as a function of antenna beam widening n (see text and Figure 1). Results are presented for three SNR orders of magnitude and 1024 looks; typical ERS SNR ranges from 10 to 100 over land. Published range for pixel-offset analysis is denoted as a pink line, using values from *Jonsson et al.* [2002].

backward looking interferograms. In addition, because the angular beam width is ~0.3 degrees for ERS, and the atmospheric water vapor is concentrated below 1–2 km height, the forward- and backward-looking LOS pass through similar lower atmosphere. Specifically, any delay due to atmospheric water vapor variations of wavelength larger than ~5 meters is will also be present in both interferograms, assuming that water vapor is concentrated in the first 1km of the troposphere. Therefore phase contributions from these factors cancel in the differential interferogram, leaving only the along-track displacement term.

[14] The new technique therefore provides the along-track component directly. MAI can be applied to other InSAR systems, such as RADARSAT, JERS, Envisat and ALOS.

3. Application

[15] We applied our method to InSAR analysis of the Mw 7.1 1999 California, Hector Mine earthquake, because GPS and offset-derived displacements are available [*Agnew et al.*, 2002; *Jonsson et al.*, 2002; *Fialko et al.*, 2001]. We used the descending orbits pair of 23027, September 15, 1999 and 23528, October 20, 1999, track 127, frame 2907, both acquired by the ERS-2 satellite, with perpendicular baseline of 21 m.

[16] We implement the MAI algorithm using conventional InSAR software (range-Doppler processing), steering the beam by modifying the Doppler centroid f_{DC}, and limiting the integration time to the appropriate interval. We estimate a minimum SNR of 76 from comparing brightness in different parts of the conventionally processed SAR images, and therefore use a beam-widening of $n = 0.6$, and 0.4 times the total integration time. The modified Doppler centroids are $f_M = f_{DC} \pm n \cdot \frac{v}{l}$, where v is the effective velocity of the satellite. To map the MAI phase changes to along-track displacements we account for the change in LOS direction across the swath.

[17] The results (Figure 3a) show a similar pattern to the pixel offset analysis displacements from *Fialko et al.* [2001] (Figure 3b). To better visualize the differences we also plot the displacements using a color scale of ±1 m (Figures 3c

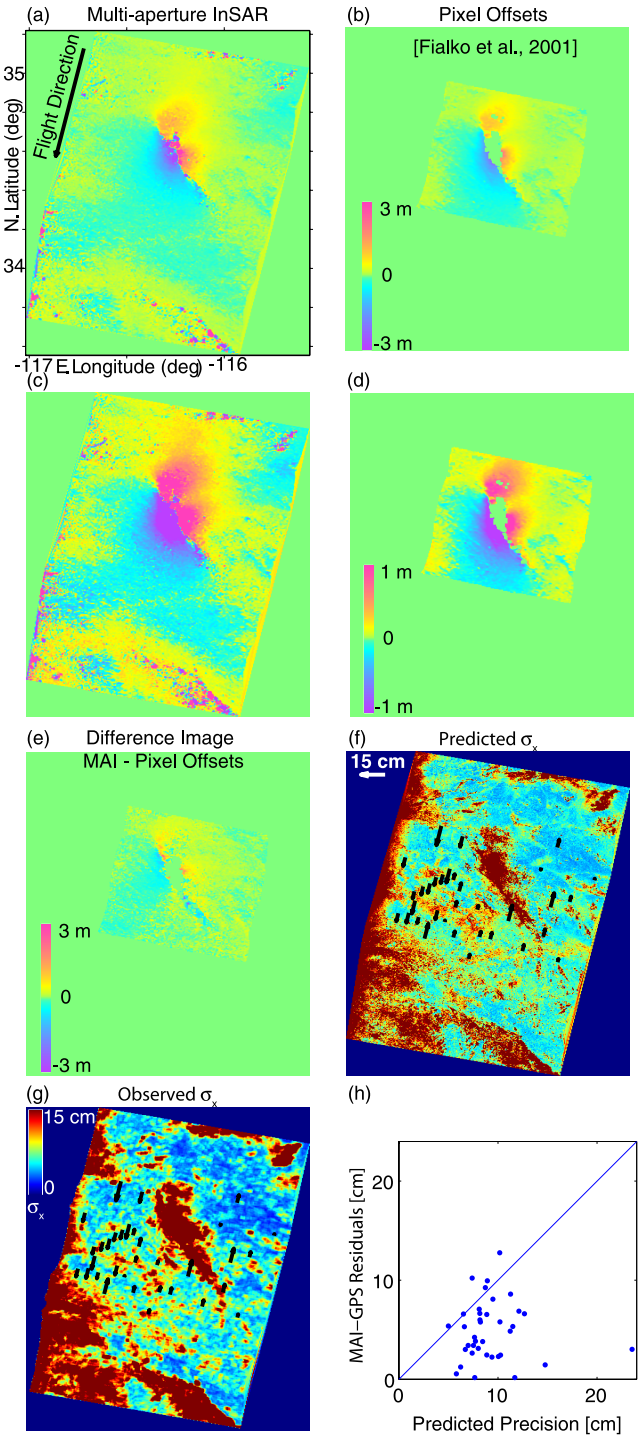

Figure 3. MAI displacements, and comparison to other methods. All sub-figures cover the same area. (a, b) MAI and pixel-offset [*Fialko et al.*, 2001] displacements for the Hector Mine earthquake. Displacements are in the along-track direction, which is denoted by a black arrow. (c, d) same as Figures 3a and 3b, with scale ±1 m. (e) Difference plot of MAI minus pixel-offset measurements. The RMS of the difference between the two measurements is 22.6 cm. (f) Theoretical and (g) observed precision of the new method. Arrows denote difference between GPS and MAI, plotted in the along-track direction. The predicted σ_x was calculated from the InSAR coherence image and equation (5), and a lower bound on SNR. We obtained a minimum SNR estimate of 76 from the power ratio between a dark and a bright area in the SAR images. The predicted σ_x therefore represents an upper bound. (The) observed σ_x is calculated over 10x10 pixel windows. The map appears to have a cruder resolution due to the windowing effect. Note that in some parts of the image the observed σ_x betters the theoretical bound, likely due to SNR variations. (h) Predicted precision versus actual GPS-MAI residuals, for GPS data collected up to two months after the earthquake. Note that the residuals equal or better the theoretical standard deviation for most GPS sites. The GPS-MAI residual for GPS site CHUK (not shown) is −1.39 m, however the predicted error is 55 cm. The projected GPS displacement at CHUCK is 2.1 m. This discrepancy suggests an upper bound of ≤2 m on the maximum deformation that can be measured with MAI.

and 3d). Note that MAI shows a larger spatial extent of deformation. Note in Figure 3d that the pixel-offset result shows a value of ~10 cm in the far-field. In order to plot the difference between the two results we first subtract this value from the pixel-offset result, and then calculate the difference (Figure 3e). The MAI algorithm yields larger absolute displacement values than the azimuth offset calculation in all but the south-west deformation side-lobe. The RMS of the difference between the two measurements is 22.6 cm.

[18] We calculate the expected error in the MAI displacements using equations (5), modified for n = 0.6, equation (6), and (6), and the measured interferogram coherence. The theoretical standard deviation map (Figure 3f) agrees with the experimentally measured standard deviation of displacements (Figure 3g) within 8 cm. The observed precision betters the theoretical limit in some areas likely because we used a lower bound on the SNR. In areas with high coherence (>0.8), measurement standard deviation ranges from 2 to 4 cm. A coherence of 0.6 corresponds to ~8 cm. A coherence of 0.4 leads to ~10 cm, and still lower coherence leads to >15 cm standard deviation.

[19] We also compare the MAI displacements with GPS observations from *Agnew et al.* [2002], projected on the along-track direction. The GPS sites are distributed in areas with MAI precision of 5 to 24 cm, therefore providing a way to test the accuracy of the new method in this range. In Figure 3h we present the predicted precision plotted against the GPS-MAI residuals. For 84% of the GPS sites, the predicted precision is equal or better than the actual errors. We plot MAI displacements at the 68% confidence level against the GPS displacements in Figure 4a. The root mean square (RMS) error between the GPS and the MAI displacements is 8.8 cm all GPS receivers, and the slope of the least-squares line fit between them is 1.

[20] The InSAR and MAI interferograms represent cumulative displacements from the earthquake and 4 days of post seismic deformation. The GPS displacements, on the other hand, span different time periods, with about half the sites (30) including post-seismic deformation spanning 6 and 3 months after the earthquake, with up to 3cm displacements [*Agnew et al.*, 2002]. A better comparison is therefore to compare displacements taken at the same time. We compare in Figure 4b the MAI displacements with GPS displacements spanning the earthquake and up to two months after the earthquake. The RMS error now drops to 6.9 cm. Tighter time constraints (2 weeks) can drop the RMS error down to 5 cm, however then the best fit slope changes to 0.8, possibly due to bias caused by the location of the GPS sites. We estimate that the new method's precision for the Hector Mine earthquake is about 5.5–6.5 cm for the descending orbit pair.

[21] In Figure 4c we display the GPS and MAI+InSAR vectors in a horizontal grid, with the new along-track horizontal vector oriented in its true direction, and the conventional LOS magnitude drawn perpendicular to it. We plot the GPS displacements corresponding to up to 2 months after the earthquake on the InSAR grid, projected into the same directions. We note the similarity in direction and magnitude. The 3-dimensional GPS displacements are projected to the LOS and along track directions;

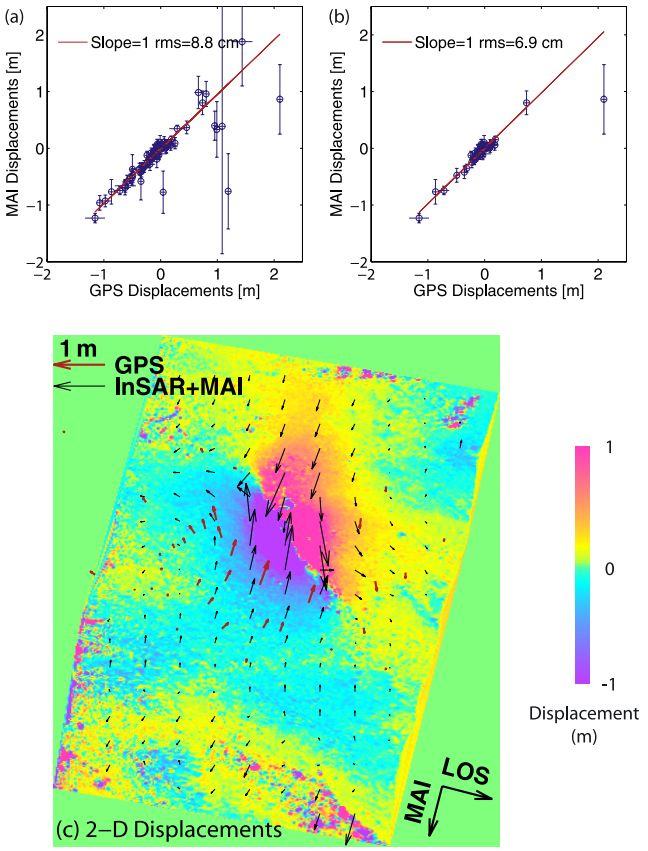

Figure 4. Comparison between MAI and GPS displacements. GPS displacements are by Agnew et al., 2001. In Figures 4a and 4b GPS and MAI displacements are plotted in the horizontal and vertical axes, respectively. Circles with bars denote MAI displacements with error bars at 68% confidence level. The red line is the best-fit least squares line, whose slope is 1 in both figures. (a) Comparison using all 71 available GPS data in the imaged area, about 30 of which were gathered 6 months after the earthquake. The RMS error is 8.8 cm and includes up to 3 cm of post-seismic displacements. This is significantly less than 15cm published by *Jonsson et al.* [2002] and *Fialko et al.* [2001] for both ascending and descending orbits. (b) Same comparison, using GPS sites that were operated up to 2 months after the earthquake. The rms error here is 6.9 cm, reduces to 6.3cm without the outlier, and may be still biased by some post-seismic deformation. (c) Vector-plot with InSAR LOS and MAI along-track displacements (black arrows) and GPS displacements up to 2 months after the earthquake (red arrows). Vector directions correspond to the along-track direction and LOS plotted in the perpendicular direction. Because the GPS displacements were projected to the LOS and along-track directions, the larger uncertainties in the GPS vertical displacements were propagated into the LOS projection, and may account for some of the variation in that direction.

it is possible that large uncertainties in the GPS vertical may contribute to differences between InSAR and GPS displacements in the LOS direction. Because many of the GPS sites are located in areas of low coherence, we suspect that the precision derived from the MAI/GPS

comparison may underestimate the performance of the new method.

4. Conclusions

[22] Using the new technique, InSAR provides two displacement vectors per interferometric pair. Hence, InSAR, conventionally thought of as a 1-D measurement, in fact contains 2-D phase information that can be extracted using split-beam processing.

[23] The new method, multiple aperture InSAR (MAI), reveals 2-D displacements per interferogram as applied to measurements of the 1999 Hector Mine earthquake coseismic deformation. The results are consistent with GPS displacements measured by *Agnew et al.* [2002], and agree qualitatively with the pixel offset analysis by *Fialko et al.* [2001]. The RMS error between the GPS and MAI displacements ranges from 5 to 6.9 cm depending on the amount of post-seismic deformation included in the GPS but missing from the InSAR data.

[24] We find that for interferogram coherence of 0.4 and higher, with SNR of 30 and higher, MAI out-performs the best-case precision expected from pixel-offset analysis.

[25] MAI is easy to implement using conventional InSAR software, and is applicable to interferograms with along-track oriented displacements, such as ERS and Envisat observations along the San-Andreas fault system. Its increased precision over existing offset-derived along-track displacements makes it a useful tool for analyzing many deformation fields.

[26] **Acknowledgments.** This study was supported by the Hal Dean fellowship in the School of Earth Sciences, Stanford University. We thank Andy Hooper, Piyush Agram, and Lauren Wye for helpful comments and discussions. Thanks are also due to Sjonni Jonsson and Yuri Fialko for the pixel-offset results. We are grateful to Roland Burgmann for early reviews of this manuscript and to Gareth Funning and an anonymous reviewer for thoughtful comments. Data were provided by the European Space Agency.

References

Agnew, D. C., S. Owen, Z. K. Shen, G. Anderson, J. Svarc, H. Johnson, K. E. Austin, and R. Reilinger (2002), Stress field variations in the Swiss Alps and the northern Alpine foreland derived from inversion of fault plane solutions, *Bull. Seismol. Soc. Am.*, *92*(4), 1355–1364.

Fialko, Y. (2004), Probing the mechanical properties of seismically active crust with space geodesy: Study of the coseismic deformation due to the 1992 M_w 7.3 Landers (southern California) earthquake, *J. Geophys. Res.*, *109*, B03307, doi:10.1029/2003JB002756.

Fialko, Y., M. Simons, and D. Agnew (2001), The complete (3-D) surface displacement field in the epicentral area of the 1999 M_w 7.1 Hector Mine earthquake, California, from space geodetic observations, *Geophys. Res. Lett.*, *28*(16), 3063–3066.

Fialko, Y., D. Sandwell, M. Simons, and P. Rosen (2005), Three dimensional deformation caused by the Bam, Iran, earthquake and the origin of the shallow slip deficit, *Nature*, *435*, 295–299, doi:10.1038/nature03425.

Froger, J. L., Y. Fukushimana, P. Briole, T. Staudachr, T. Souriot, and N. Villneuve (2004), The deformation field of the August 2003 eruption at Piton de la Fournaise, Reunion Island, mapped by ASAR interferometry, *Geophys. Res. Lett.*, *31*, L14601, doi:10.1029/2004GL020479.

Funning, G. J., B. Parsons, T. J. Wright, J. A. Jackson, and E. J. Fielding (2005), Surface displacements and source parameters of the 2003 Bam (Iran) earthquake from Envisat advanced synthetic aperture radar imagery, *J. Geophys. Res.*, *110*, B09406, doi:10.1029/2004JB003338.

Jonsson, S., H. Zebker, P. Segall, and F. Amelung (2002), Fault slip distribution of the M w 7.1 Hector Mine, California, earthquake, estimated from satellite radar and GPS measurements, *Bull. Seismol. Soc. Am.*, *92*(4), 1377–1389.

Joughin, I. R., R. Kwok, and M. A. Fahnestock (1998), Interferometric estimation of three-dimensional ice-flow using ascnding and descnding passs, *IEEE Trans. Geosci. Remote Sens.*, *36*(1), 25–37.

Michel, R., J. P. Avouac, and J. Taboury (1999a), Measuring ground displacements from SAR amplitude images: Application to the Landers earthquake, *Geophys. Res. Lett.*, *26*(7), 875–878.

Michel, R., J. P. Avouac, and J. Taboury (1999b), Measuring near field coseismic displacements from SAR images: Application to the Landers earthquake, *Geophys. Res. Lett.*, *26*(19), 3017–3020.

Peltzer, G., F. Crampe, and G. King (1999), Evidence of nonlinear elasticity of the crust from the Mw7.6 Manyi (Tibet) earthquake, *Science*, *286*, 272–276.

Rodriguez, E., and J. M. Martin (1992), Theory and design of interferometric synthetic aperture radars, *IEE Proc. Part F Radar Signal Process.*, *139*(2), 149–159.

Simons, M., Y. Fialko, and L. Rivra (2002), Co-seismic deformation from the 1999 Mw 7.1 Hector Mine, California, earthquake as inferred from InSAR and GPS observations, *Bull. Seismol. Soc. Am.*, *92*(4), 1390–1402.

Wadge, G., B. Parsons, and the Evinsar science team (2003), Achieving the EVINSAR objectives with TerraSAR-L, in *Proceedings of the FRINGE 2003 Workshop, Frascati, Italy, 1–5 Dec. 2003* [CD-ROM], edited by H. Lacoste, *Eur. Space Agency Spec. Publ.*, *ESA SP-550*.

Wright, T. J., B. E. Parsons, and Z. Lu (2004), Toward mapping surface deformation in three dimensions using InSAR, *Geophys. Res. Lett.*, *31*, L01607, doi:10.1029/2003GL018827.

Zebker, H. A., and J. Villasenor (1992), Decorrelation in interferomtric radar echos, *IEEE Trans. Geosci. Remote Sens.*, *30*, 950–959.

N. B. D. Bechor and H. A. Zebker, Department of Geophysics, Stanford University, Mitchell Building #360, Stanford, CA 94305, USA. (nbechor@pangea.stanford.edu)